Reviews of Electromagnetics, Vol. IV, 2025
EuCAP 2025 Special Issue
DOI: 10.53792/RoE/2025/25014

Reviews of Electromagnetics
EuCAP 2025 Special Issue

# Efficient Compact Single-Layer Metasurface RF Energy Harvesters for IoT Applications

Raziyeh Sharifi[1]*, Anne Claire Lepage[1], Kyriaki Niotaki[1], Xavier Begaud[1]

**Abstract**
In this paper, we extend our previous works on compact and efficient metasurface energy harvesters by introducing additional theoretical analysis, and measurement results for evaluating performance in finite arrays. Two metasurface harvesters are studied: a single-band design operating at 2.45 GHz and a dual-band design covering 2.45 GHz and 5.2 GHz (Wi-Fi bands), proposed for IoT applications. This paper introduces the concept of central rows in the finite array, which provides a more realistic and reliable metric for characterizing the capturing efficiency. For both designs, 5×4 finite arrays are analyzed. The simulated capturing efficiency of the central rows reaches 90% at 2.54 GHz for the single-band structure, and 74% at 2.5 GHz and 30% at 5.09 GHz for the dual-band design. Each proposed design has been analyzed independently, fabricated, and measured to verify its performance.

**Key terms**
Metasurface; Energy harvester; Radio frequency; Wi-Fi; IoT applications

[1] *LTCI, Télécom Paris, Institut Polytechnique de Paris, Palaiseau, France*
*__Corresponding author__: raziyeh.sharifi@ieee.org

Received: 23/05/2025, Accepted: 22/09/2025, Published: 28/11/2025

## 1. Introduction

RF Energy harvesting refers to the process of collecting energy from ambient sources and transforming it for storage or to power a wide variety of applications. The purpose of this work is to propose an efficient device to collect ambient radio frequency (RF) energy, such as that found in the signals emitted by wireless routers. Although the ambient RF power level is comparatively low in comparison to solar and wind power, it is widely available and can be sufficient to support modest power requirements such as those of internet of things (IoT) devices; it may also supplement primary power supplies such as batteries. Wi-Fi signals at 2.45 GHz and 5.2 GHz (IEEE 802.11ax/be) represent one of the most accessible and widely available sources for RF energy harvesting in modern life [1], [2]. These frequencies are commonly found in environments such as homes, offices, and public spaces such as train stations, as well as outdoor areas where Wi-Fi networks are freely accessible such as in the city of Luxembourg.

An RF energy harvester typically comprises two essential components, a receiver and a rectifier circuit. The receiver is responsible for capturing RF energy from the surrounding environment, ensuring efficient energy collection. To facilitate the collection of ambient RF energy, so-called metasurfaces can be employed. These are purpose-engineered materials (metamaterials) with favorable properties that allow for near-complete absorption of the incident RF power. In addition to their high absorption potential, another key feature of metasurface absorbers is their low thickness [3]–[5]. Commonly, to design a metasurface harvester, first the rectifier circuit is replaced by the equivalent resistive load. The objective is to design the metasurface, acting as the receiver, such that the maximum ambient RF energy is collected in this resistive load. Second, in the final design the resistive load is replaced with a suitable rectifier to convert collected RF power to DC. The capturing efficiency of the metasurface harvester can be defined as below:

$$\eta_{\mathrm{MS}} = \frac{P_{\mathrm{dl}}}{P_{\mathrm{in}}} \tag{1}$$

where $P_{\mathrm{dl}}$ is the power delivered to the resistive load of the metasurface, and $P_{\mathrm{in}}$ is the incident power over the metasurface area. The placement of the resistive load depends on the metasurface configuration. In multilayer metasurface harvesters, the load is typically located in an additional layer [6]–[8]. Multi layers configuration increases design complexity and introduces fabrication challenges. In contrast, planar designs simplify implementation by placing the resistive load on the same layer as the metasurface, thereby reducing fabrication difficulty and

system complexity. One promising technique within planar metasurface designs is the interconnected cells method [9]–[13]. This approach allows multiple unit cells to be connected to each other, forming a "supercell". The last cell in the supercell is connected to a resistive load. Due to its larger surface area, the supercell naturally captures more RF energy than an individual cell.

The absorption characteristics and the number of operating frequencies of metasurface harvesters are influenced by the shape and the number of resonators within the structure. By combining multiple resonators of different sizes or shapes, each resonator can resonate at its individual operating frequency, allowing the structure to absorb energy at multiple distinct frequency bands. This paper builds on the foundation of our previous works on RF metasurface energy harvesters [11]–[12], where we first introduced a single-band design operating at 2.45 GHz, followed by a dual-band metasurface harvester operating at 2.45 GHz and 5.2 GHz. In this paper, we expand upon those contributions by providing a comprehensive and in-depth analysis of both designs, and present the measurement results of both devices. We further detail the challenges encountered during the measurement process and propose solutions to overcome them.

Aiming for a compact and simple design, the interconnected cells method has been selected as a promising technique to achieve a planar metasurface RF energy harvester in this work. However, enhancing its capturing efficiency remains challenging while minimizing the number of lumped elements used in the metasurface design. In the following section, first the single-band design will be discussed as a foundation before presenting the dual-band structure in detail. Each design in this paper contains four main steps. First, the unit cell design is presented; second, the supercell discussion is detailed, and an intermediate step in the design process of the metasurface harvester is proposed to enhance its capturing efficiency. Following this, a finite array is proposed and discussed. Then, the measurement result of the fabricated proposed structure is presented.

## 2. Single-band Designs

### 2.1. Unit cell Design M1 and M2

Metasurfaces are generally periodic structures composed of unit cells designed to manipulate electromagnetic waves. In this paper, first the single-band unit cell geometry is carefully designed and optimized to absorb most of the incident RF energy while being compact and simple. As mentioned in the introduction, the design of our proposed dual-band metasurface harvester is developed based on a single-band metasurface harvester initially optimized to operate at 2.45 GHz. Then a second single-band design is optimized to operate at 5.2 GHz, and after both designs are combined to achieve dual-band performance (Section III). The single-band metasurface harvesters are labeled as "M1" and "M2" in Fig. 1a and Fig. 1b, respectively and are operating at 2.45 GHz and 5.2 GHz, respectively. The top layer of the proposed unit cells is composed of two rectangular metallic rings facing each other, separated by a gap of width "$g$", the corresponding parameters are provided in Table. 1. In the interconnected cells method, adjacent unit cells are connected to one another [9]–[13]. Accordingly, in the proposed unit cell design, the two microstrip lines along the $x$-axis are located in the middle of the unit cell, each attached to its respective ring, as shown in Fig. 1.

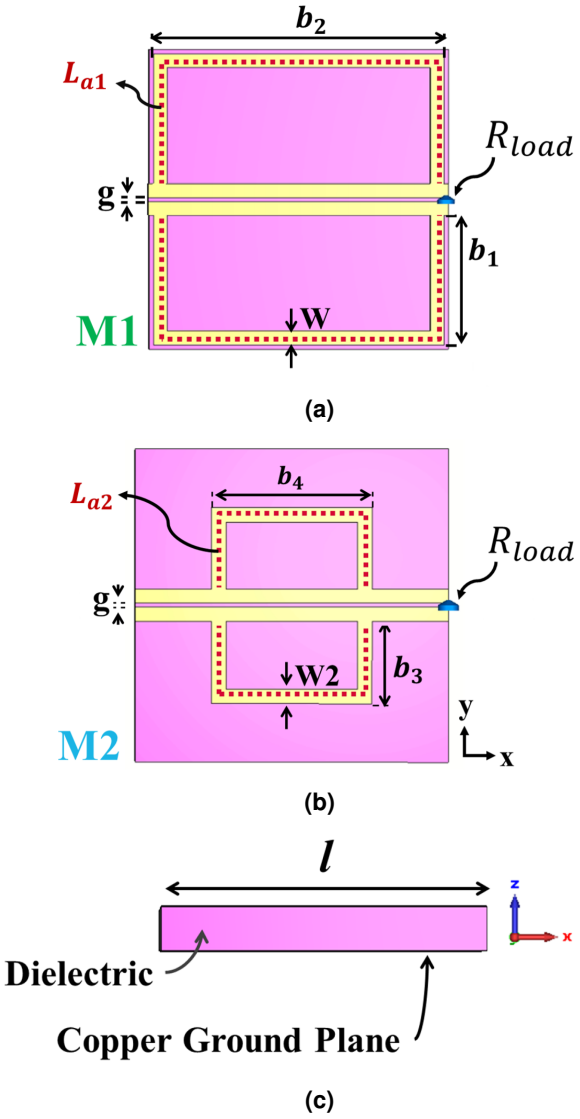


**Figure 1:** Geometry of the proposed single-band unit cell operating at (a) 2.45 GHz (b) 5.2 GHz and (c) side view ($l$=27.3 mm, and g=0.35 mm).

For electromagnetic waves to be absorbed efficiently by a metasurface, its surface impedance must match that of free space. The goal is to increase the amount of usable energy collected and not let the absorbed energy be dissipated in the substrate. As a result, a low-loss dielectric should be chosen. Arlon DiClad 880, with permittivity equal to 2.17, a loss tangent of 0.0009, and a thickness of 2.36 mm, has been chosen as the substrate due to the desired low-loss property [14] and its availability in the lab. To satisfy the impedance matching between the metasurface harvester and free space, the resistive load ($R_{\text{load}}$) is introduced into each design. Note that the resistive load not only facilitates impedance matching but also

serves as an energy collection element within the metasurface. The resistive load in the EM model is implemented as an ideal lumped element using CST's built-in library. This simplification does not account for parasitic effects. As explained in this introduction, this load will be replaced by a rectifier circuit later in order to finalize the energy harvester design. The values of the resistive load are obtained for each design by optimizing the collected power in the load at the targeted frequency. The periodicity of the metasurface unit cell is 0.22 $\lambda_0$ at 2.45 GHz, and 0.47 $\lambda_0$ at 5.2 GHz ($\lambda_0$ is free space wavelength).

In Fig. 1a, for M1, the rectangular rings have inner and outer lengths of $b_1$-$W$ and $b_1$ along the y-axis, and $b_2$-$W$ and $b_2$ along the x-axis, respectively. Fig. 1a indicates, with a red dashed line, the average length $L_{a1}$ of the inner and outer ring. $L_{a1}$ comprises the lengths of two rectangular rings, excluding the two microstrip lines in the middle and the gap "g" between them; see Eq. 2. Similar to the discussion for M1, for M2 the rectangular rings have inner and outer lengths of $b_3$-$W_2$ and $b_3$ along the y-axis, and $b_4$-$W_2$ and $b_4$ along the x-axis, respectively. The average of these inner and outer lengths is denoted by the red dashed line ($L_{a2}$) in Fig. 1b. In calculating this length, the widths of the two microstrip lines in the middle and the gap "g" between them are subtracted as depicted in Eq. 3.

$$L_{a1} = 4 \times b_1 + 2 \times b_2 - 4 \times W \tag{2}$$

$$L_{a2} = 4 \times b_3 + 2 \times b_4 - 4 \times W_2. \tag{3}$$

The dimensions of the M1 and M2 geometry are computed so that half the length of La1 and La2 closely approximates the half-guided wavelength at 2.45 GHz and 5.2 GHz. Subsequently, the design parameters are optimized to achieve maximum capturing efficiency at these frequencies. The half-guided wavelength at the resonant frequencies of 2.45 GHz ($\sim$ 46.82 mm) and 5.2 GHz ($\sim$ 22.06 mm) are calculated according to [17]

$$\lambda_g = \frac{C}{f\sqrt{\varepsilon_e}} \tag{4}$$

where $C$ is the speed of light, $f$ is the resonance frequency, and the effective permittivity $\varepsilon_e$ is approximately 1.71 and is obtained according to the formula below [17]:

$$\varepsilon_e = \frac{\varepsilon_r + 1}{2} + \frac{\varepsilon_r - 1}{2} F\left(\frac{W}{h}\right) - \frac{\varepsilon_r - 1}{4.6} \cdot \frac{t/h}{\sqrt{W/h}} \tag{5}$$

$$F\left(\frac{W}{h}\right) = \begin{cases} \left(1 + \dfrac{12h}{W}\right)^{-0.5} + 0.04\left(1 - \dfrac{W}{h}\right)^2, & \text{if } \dfrac{W}{h} \le 1 \\ \left(1 + \dfrac{12h}{W}\right)^{-0.5}, & \text{if } \dfrac{W}{h} \ge 1 \end{cases} \tag{6}$$

with $W$ and $h$ denoting the width of the microstrip lines and the thickness of the substrate, respectively; $t$ denoting the thickness of the copper; and $\varepsilon_r$ being the relative permittivity of the substrate. Note that the design corresponds to the $W/h \le 1$ regime of Eq. 6. It is worth mentioning that if the mutual coupling between adjacent cells is too strong, it can influence the resonance frequency, causing it to deviate slightly from the expected value based on $L_{a1}$ and $L_{a2}$. The final optimized parameters, as presented in Table. 1, result in a half-length of $L_{a1}$ and $L_{a2}$ equal to 47.58 mm and 25.68 mm respectively —values that are close to the half-guided wavelength at 2.45 GHz and 5.2 GHz.

**Table 1:** Design parameters and load resistance

| Design | $b_1$ (mm) | $b_2$ (mm) | $b_3$ (mm) | $b_4$ (mm) | $R_{\text{load}}$ ($\Omega$) | $W = W_2$ (mm) |
|---|---|---|---|---|---|---|
| M1 | 11.8 | 26.5 | - | - | 700 | 1.26 |
| M2 | - | - | 7.1 | 14 | 250 | 1.26 |

The polarization of the incident plane wave is along the y-axis. The design and optimization of the proposed metasurface are obtained using the EM simulation software CST Studio Suite, with a full-wave frequency domain solver. It is important to mention that the unit cell is simulated under periodic boundary conditions for emulating the infinite array in the x-y plane while a normal incident plane wave illuminates the structure in direction of the –z-axis. Fig. 2 shows the simulated efficiencies of the single-band unit cell of the metasurface harvesters M1 and M2, respectively. The proposed design operates in a single polarization and has the advantage of simplicity. The proposed scenario is that the device is used to capture Wi-Fi signals in a same room as the transmitting antennas or in neighboring rooms at the same floor. In this Wi-Fi scenario, the router or base station antennas are positioned vertically (vertical polarization) for a broader horizontal range, then the device must be placed to capture this vertical polarization.

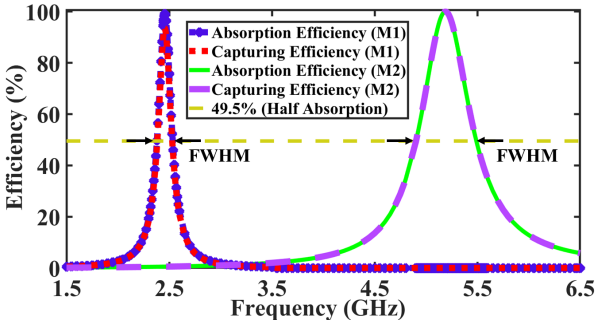


**Figure 2:** Individually simulated efficiencies for M1 and, M2.

The absorption and capturing efficiencies of M1 are 99% and 94% at 2.45 GHz, whereas, for M2, they are 99% and 96% at 5.2 GHz. Thus, less than 5% of the absorbed energy is dissipated in the substrate for the M1 design, and less than 3% for the M2 design.

The full width at half maximum (FWHM) absorption bandwidths ($\Delta f$) are 0.154 GHz (2.38 to 2.534 GHz) for M1 and 0.59 GHz (4.9 to 5.49 GHz) for M2, as shown in Fig. 2. The Q-factor of each resonator M1 and M2 can be calculated by the equation below [18, 19].

$$Q(f) = \frac{f}{\Delta f}. \tag{7}$$

In this equation, f is the resonance frequency where the maximum absorption occurs. The Q-factor is introduced here as a metric to assess the broadband absorption characteristics of the design. The Q-factors for M1 and M2, with the corresponding center frequencies of 2.45 GHz (f1) and 5.2 GHz (f2), are 16 and 9, respectively. Q(f1) has a lower value compared to Q(f2), which demonstrates that M1 has sharper resonance compared to M2.

The single-band design M2 demonstrates a wider absorption bandwidth compared to M1, which can be attributed to both designs maintaining the same line width ($W = W_2$) as seen in Fig. 2. Typically, as the operating frequency increases, the dimensions of the corresponding resonator must decrease to preserve the absorption bandwidth.

Since both M1 and M2 follow the same design process, the following discussion will focus on M1. Fig. 3 depicts the distribution of the surface current of the proposed unit cell (M1) at 2.45 GHz; from simulations at other frequencies, it can be concluded that the strongest current does indeed occur at 2.45 GHz. The two red arrows in Fig. 3 represent the observed resonances. Each of these arrows extending between the two purple stars indicates the current amplitude going from least to highest (in the center) and again back to least. The length $L_r$ of each resonance equals half the length of $L_{a1}$:

$$L_r = 2 \times b_1 + b_2 - 2 \times W = 47.58 \text{ mm}. \quad (8)$$

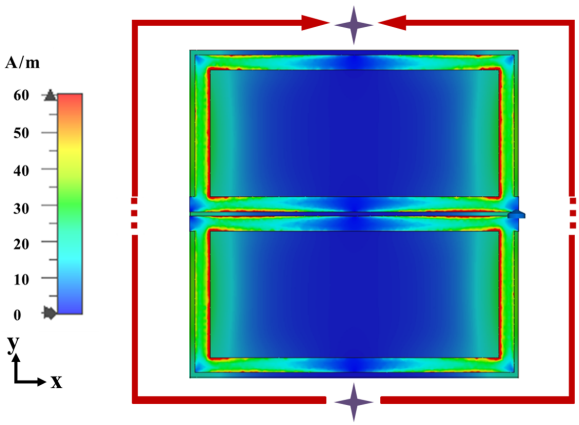


**Figure 3:** Surface current distribution at 2.45 GHz; the resonance is indicated with the red arrows. (The dashed lines do not contribute to the length of $L_r$.)

Following the unit cell design, the metasurface supercell design is the next step.

## 2.2. Supercell Design M1

The supercell of the proposed metasurface harvester comprises four interconnected cells (N=4) along the x-axis, where a single resistive load with the initial value of 700 Ω (see Table. 1) is placed at the end of the microstrip lines (in the gap) of the proposed metasurface unit cell. The supercell is designed in CST Studio Suite under periodic boundary conditions on both the x-axis and the y-axis as shown in Fig. 4.

Keeping the resistive load value of the supercell the same as the unit cell, causes its capturing efficiency drops compared to

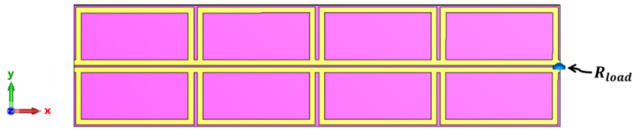


**Figure 4:** Schematic of the proposed supercell.

that of the unit cell. This is due to the mismatched impedance between free space and the supercell, as the initial unit cell design was based on each cell being individually connected to a resistive load (recall that the simulation took place under periodic boundary conditions). The absorption features of the proposed metasurface structure are defined by the geometry of the metallic rings, the resistive load value, and the substrate characteristics. Taking all of this into account, an additional intermediate optimization step in the supercell design is proposed, which is to reoptimize the resistive load value through a parameter study. The obtained optimum resistive load value is 115 Ω. The capturing efficiency of the single-band supercell with the optimum load compared to the one with the initial load value enhanced from 62% at 2.45 GHz to 92% at 2.49 GHz. A slight frequency shift between the unit cell and the supercell simulation occurs because of the adjusted load value; this shift can be mitigated by adjusting the dimensions of the rectangular rings.

## 2.3. Finite Array Design M1

For the final simulation step in the metasurface design, a finite array, depicted in 5, containing 5 rows of 4 cells each (5 rows; Middle Row, Row 1, and Row 2, with the latter two replicated across the middle row) was simulated with CST Studio Suite using the time domain (TD) solver, under plane wave excitation. A resistive load of 115 Ω is positioned at the end of each of the five rows. The choice of this resistance value comes from the optimization of the supercell (N=4). The choice of the size of the array depends on several factors, such as the maximum allowed device size for an intended application, the level of available input power, etc.

To the best of the author's knowledge, in the works on the interconnected cells method presented in [9]–[11], only one rectifier is placed at the end of the middle row. The total efficiency of the metasurface and the rectifier is evaluated on the middle row only. Thus, the incident power arriving on the middle row's surface is considered. However, going further than these works, we not only analyze the middle row of the metasurface independently, that is, aside from the rectifier, but also the other rows in detail. This leads us to introduce the concept of "central rows" to evaluate the performance of the metasurface harvester with higher accuracy. We shall first explain this concept in detail and thereafter discuss the motivation behind its introduction.

The capturing efficiency of the finite array of the proposed metasurface can be calculated by Eq. 1, where $P_{\text{in}}$ is obtained by integrating the Poynting vector over the metasurface footprint. Fig. 6 shows the comparison between the simulated capturing efficiency of each row (surface area equal to $0.00298\,\text{m}^2$) with

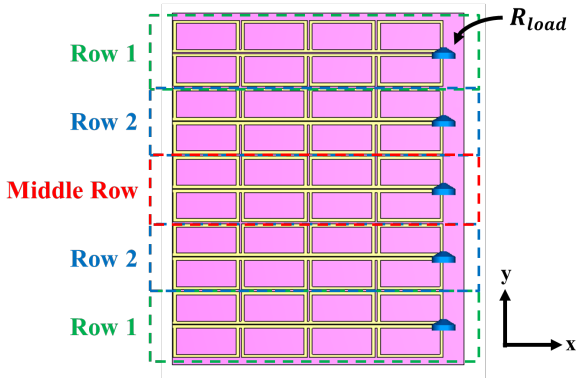


**Figure 5:** Proposed finite array with row labels.

the initial and reoptimized resistive load values. The capturing efficiencies plotted in Fig. 6 are tabulated in Table. 2.

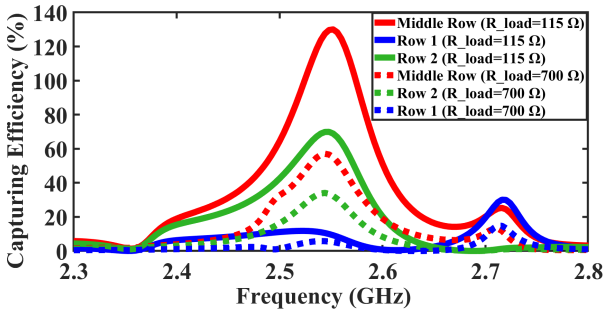


**Figure 6:** Comparison between the simulated capturing efficiency of different rows for the initial $R_{\text{load}}$ (700 Ω) and the reoptimized $R_{\text{load}}$ (115 Ω).

Two key points can be derived from the comparative plots in Fig. 6.

**Table 2:** Capturing efficiencies for different rows at 700 Ω and 115 Ω.

| Row number | Frequency (GHz) | $\eta_{\text{MS}}$ (%) | $R_{\text{load}}$ (Ω) |
|---|---|---|---|
| 1 | 2.54 | 6 | 700 |
| 2 | 2.54 | 34 | 700 |
| Middle | 2.54 | 57 | 700 |
| 1 | 2.52 | 12 | 115 |
| 2 | 2.54 | 70 | 115 |
| Middle | 2.54 | 130 | 115 |

First, it can be seen that the capturing efficiency varies across the rows, with the middle row having the highest. Second, it shows the increase of the capturing efficiency of each row when reoptimizing the resistive load value. Regarding the second point above, it is important to note the difference between the supercell and finite array simulation conditions. When a supercell is simulated in periodic boundary conditions, an infinite number of supercells are positioned next to each other; as a result, there is a uniform mutual coupling among them. However, when simulating the finite array, the power distribution within the array is affected by the non-uniform mutual coupling among the cells. As a result, the middle row witnesses a higher collected power in comparison with the other rows; this is not only due to absorbing the direct incident power but also due to the coupled power from the adjacent rows around the middle one. This is demonstrated by the efficiency of the middle row (Fig. 6) which exceeds 100%! However, the capturing efficiency of the whole array is 58%. We must therefore take care to consider more than only the middle row for evaluating the performance of the final metasurface harvester. Indeed, as the edge rows are less efficient than the others (due to the absence of adjacent rows on each side), a sufficient number of central rows (the rows around and including the middle row) are required. Accordingly, the proposed finite array comprises five rows, of which the three central rows have the most similarity to the supercell simulation conditions. So, to have a more accurate conclusion on the performance of the proposed metasurface, we calculate the capturing efficiency of the central rows, which is more informative in comparison with previous works [9]–[13] where only the middle row of the whole structure was considered.

The capturing efficiency of the central rows is equal to

$$\eta_c = \frac{P_{\text{dl-2}} + P_{\text{dl-m}} + P_{\text{dl-2}}}{3 \times P_{\text{in-r}}} \tag{9}$$

where $P_{\text{dl-2}}$, and $P_{\text{dl-m}}$ indicate the power delivered to the resistive load of the Row 2 and middle row of the metasurface. The incident power over the surface area of the central rows, equals three times the incident power of a single row, $P_{\text{in-r}}$. Note that $P_{\text{in-r}}$ has the same value for all rows, as their surface areas are equal. Eq.9 can be simplified to the average efficiency of the three central rows:

$$\eta_c = \frac{\eta_2 + \eta_m + \eta_2}{3} \tag{10}$$

where $\eta_2$ and $\eta_m$ are the capturing efficiencies of Row 2 and the middle row, respectively. As a result the central rows can be treated as an average row, a terminology that we introduce to emphasize that we treat the three central rows as a single row when referring to their averaged capturing efficiency. Fig. 7 depicts a comparison between the simulated capturing efficiency of the average row of the metasurface array, using the initial resistive load value of 700 Ω and the reoptimized value of 115 Ω. It can be seen that the capturing efficiency of the average row of the finite array improved by 50% (from 40% to 90%) at 2.54 GHz.

The next step is to measure the metasurface in order to validate its behavior.

### 2.4. Realization and Measurement Design M1

In order to evaluate the capturing efficiency of the designed metasurface harvester at the operating frequency, the collected power in the resistive load of the finite array needs to be measured. However, due to the limitations of the conventional RF measurement instruments and the geometry of the proposed structure, it is necessary to introduce a few modifications in the metasurface design and validate them by simulation before proceeding with the measurement. The resistor is placed between two metallic strips of the upper layer. But to perform this

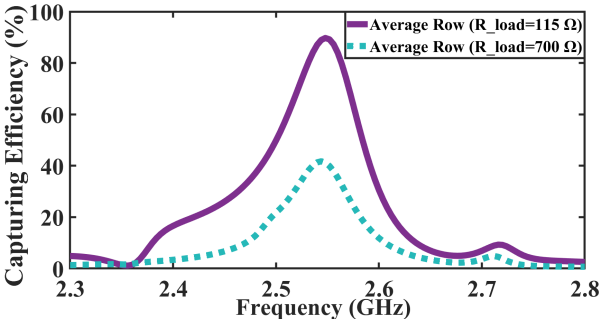


**Figure 7:** Comparison between the simulated capturing efficiencies of the average row for the optimum $R_{\text{load}}$ (115 Ω) and the initial $R_{\text{load}}$ value of the unit cell (700 Ω).

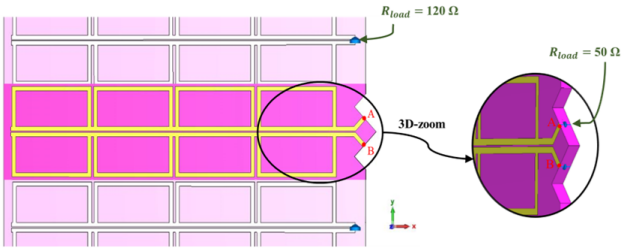


**Figure 8:** Temporary modification of the middle row of the metasurface design.

measurement, a 50 Ω power sensor (Keysight U8488A 10MHz - 67GHz power sensor) is used. As the gap between the two strips is small, the design is modified to measure the output power. It is essential to highlight that these modifications are temporary and, in the future, will not be necessary as the 115 Ω resistor will be replaced by a rectifier implemented on the same layer as the metasurface.

The adjustments to the metasurface design are restricted to its middle row, as modifying all rows would introduce significant mismatches, leading to a substantial reduction in the capturing efficiency of the metasurface finite array. Indeed, this row is less affected by edge effects and is modified to serve as a representative row to evaluate the capturing efficiency, identify the frequency at which its peak occurs, and to compare the measurement results with the simulation incorporating the same modifications. To do so, we aim to measure the RF power collected in the resistor of the middle row of the finite array, and the other rows are terminated with a 120 Ω Surface Mount Resistor (SMD). Thus, the 115 Ω load at the end of the middle row is removed, and an oblique extension of the lines is added to connect two 50 Ω SMA connectors. In the simulation, each connector is substituted with a 50 Ω load positioned between the end of the lines and the ground, as shown in Fig. 8. It is noted that the simulation has been performed while taking into account the modifications made for measurement purposes. The substrate is cut to accommodate the shape of the connectors. These modifications result in a drop in the simulated capturing efficiency of the middle row, however, their only purpose is to enable measuring RF output power and comparing the performance of the metasurface design with the simulation. The array composed of $5 \times 4$ cells with the mentioned modifications was fabricated on a 2.36 mm Arlon DiClad 880 dielectric substrate, as illustrated in Fig. 9a; the copper thickness is 0.035 mm, and the area of the substrate is $141.5 \times 121$ mm$^2$.

The measurement setup in the anechoic chamber is depicted in Fig 9b . A horn antenna illuminates the fabricated metasurface as shown in Fig 9b. The measurement configuration parameters at 2.54 GHz are provided in Table. 3. The incident power on the middle row of the metasurface design is obtained by the Friis formula:

$$P_{\text{in}} = \frac{G_{\text{h}} P_{\text{s}}}{4\pi R^2} \times A_{\text{s}}. \tag{11}$$

$G_{\text{h}}$ is the gain of the horn, and $P_{\text{s}}$ is the emitted power; $R$ is the distance between the horn and the prototype (2.39 m); and $A_{\text{s}}$ is the area of the middle row as it is explained before in the previous section (0.00298 m$^2$). The fabricated metasurface is located in the far field distance so that the wave emitted by the horn is locally considered a plane wave.

**Table 3:** Transmitter and Propagation Parameters

| Description | Value | Unit |
|---|---|---|
| Gain of the horn at 2.54 GHz | 6.5 | dBi |
| Emitted power measured at the horn input | 24.4 | dBm |

The capturing efficiency of the fabricated metasurface harvester is obtained by Eq. 1, where the collected RF power for the middle row $P_{\text{dl}}$ is the addition of the power measured at each connector (the other being connected to a 50 Ω load). The measured capturing efficiency under normal incidence is 61% at 2.49 GHz. The observed discrepancies between the simulated and measured performance of the middle row of the finite array of the metasurface harvester can be mainly attributed to the sensitivity of the design to the parameter dimension changes (which may occur, among other reasons, due to fabrication errors). The observed change in performance could be due to the fact that by varying the design parameters, the mutual coupling between the cells is impacted. We observe that the simulated capturing efficiency of the average row resembles more closely the measured capturing efficiency of the middle row. In Fig. 10, the measured capturing efficiency of the middle row and the simulated capturing efficiency of the average row are compared. The observed agreement in Fig. 10 can be due to the mutual coupling between the cells of the middle row in the fabricated array introducing a behavior resembling that of the average row.

In Fig. 10, for the normal incidence, FWHM capturing bandwidth for the simulated average row is 0.092 GHz (2.494 to 2.586 GHz), and 0.11 GHz (2.45 to 2.56 GHz) for the measured middle row. The corresponding Q-factor of the former is 27.6 and of the latter 22.6, with the center frequencies of 2.54 GHz and 2.49 GHz, respectively. Knowing the performance of the device as a function of the angle of incidence is crucial information for the application, so Fig. 10 shows the comparison between the simulated and measured capturing efficiency of the proposed metasurface harvester at two oblique incidence angles. The corresponding data supporting a good agreement

(a)

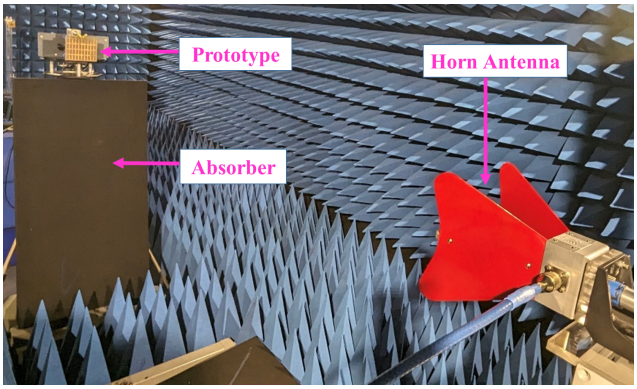


(b)

**Figure 9:** (a) Prototype of the proposed modified metasurface design with the soldered connectors (b) measurement setup in the anechoic chamber.

between measurement and simulation is given in Table. 4. As it can be seen by increasing the incidence angle, the capturing efficiency is decreasing, which shows the proposed design is sensitive over the incidence angle changes.

In conclusion, by analyzing the single-band metasurface design M1 in detail, we were able to evaluate its capturing efficiency. As a next step, the dual-band design is proposed and discussed.

## 3. Dual-band Design

### 3.1. Unit cell Design

After evaluating the performance of M1, we can now move to the next step in designing our metasurface harvester, namely, integrating the two resonators M1 and M2 into a single structure. This is done in the dual-band design shown in Fig. 11. A resistive load ($R_{load}$) is positioned at the end of the gap between the two microstrip lines. The value of the load (300 Ω) is obtained by optimizing the capturing efficiency of the design, which is a compromise between the optimum load values of the single-band designs at 2.45 GHz and 5.2 GHz. The resonance

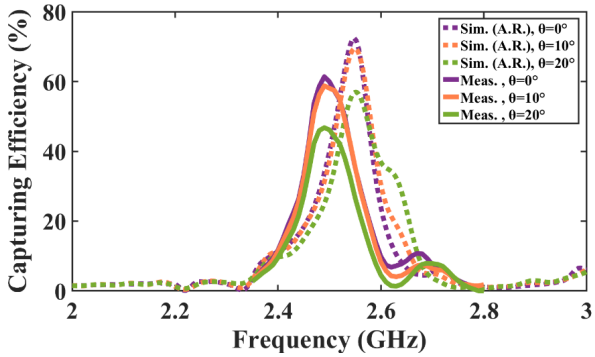


**Figure 10:** Comparison between simulated average row (A.R.) and measured capturing efficiency (middle row) at different incidence angles.

**Table 4:** Simulated (Sim) and Measured (Meas) Capturing Efficiency as a Function of the Incident Angle

| Incident angle | $\eta_{MS}$ (Sim) | Frequency (Sim) | $\eta_{MS}$ (Meas) | Frequency (Meas) |
|---|---|---|---|---|
| 0° | 73% | 2.54 GHz | 61% | 2.49 GHz |
| 10° | 69.4% | 2.54 GHz | 59% | 2.49 GHz |
| 20° | 57% | 2.55 GHz | 47% | 2.49 GHz |

frequencies of the dual-band design with the initial dimensions of M1 and M2 are 2.24 GHz and 5.12 GHz. These frequency shifts are due to the integration of M1 and M2 into a single structure with common microstrip lines. Therefore, the lengths $b_1$, $b_2$, $b_3$, and $b_4$ are slightly readjusted to account for the coupling introduced between M1 and M2. These lengths have been chosen as they can be easily adjusted without impacting the periodicity of the cell. This readjustment of the dimensions and the load value allow the proposed metasurface design to work efficiently at both targeted frequencies. The corresponding dimensions of the readjusted dual-band design are provided in Table. 5.

**Table 5:** Dual-band parameter values

| Design | $b_1$ (mm) | $b_2$ (mm) | $b_3$ (mm) | $b_4$ (mm) | $R_{load}$ (Ω) | $W = W_2$ (mm) |
|---|---|---|---|---|---|---|
| Dual-band | 11.7 | 25 | 6.9 | 13.9 | 300 | 1.26 |

The absorption efficiency of the dual-band metasurface harvester is presented in Fig. 12, reaching maxima of 94% at 2.45 GHz and 96% at 5.2 GHz. Additionally, the figure shows the capturing efficiency, with peak values of 88% at 2.45 GHz and 92% at 5.2 GHz. Therefore, the energy dissipation in the dielectric layer and metallic conductors is at most 6% for both resonance frequencies, and most of the absorbed RF energy is collected by the resistive load.

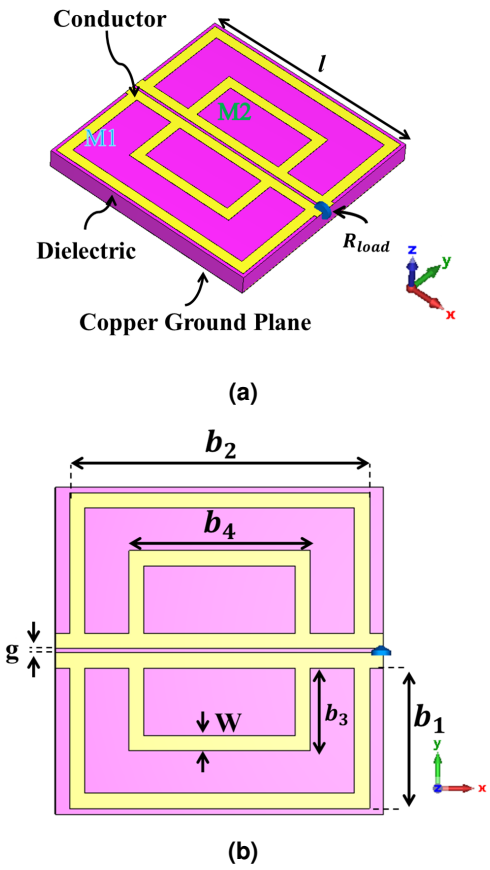


**Figure 11:** Schematic of the proposed dual-band metasurface unit cell: (a) 3-D view (b) top view ($l$=27.3 mm and g=0.35 mm).

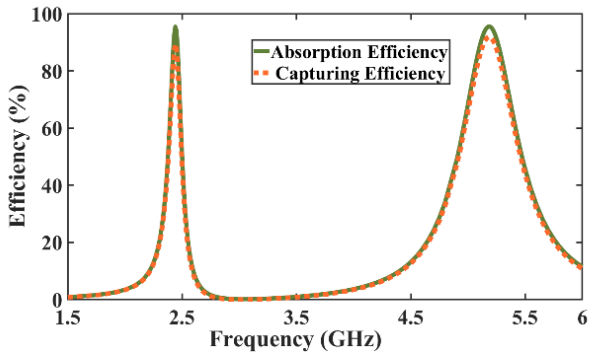


**Figure 12:** Simulated efficiencies for the dual-band metasurface harvester.

Fig. 13 illustrates the intended resonances at 2.45 GHz and 5.2 GHz, highlighting the surface current distribution. The Fig. 13a, corresponding to 2.45 GHz, shows the surface current primarily distributed along the outer ring, with two red arrows placed outside the unit cell to indicate the resonance location. The Fig. 13b, corresponding to 5.2 GHz, depicts the surface current concentrated on the inner ring, with red arrows positioned between the two rings to represent the inner ring resonance. In both subfigures, the arrows start from a purple star—representing a point of minimum current—increase to a maximum at the center, and then return to a minimum at the opposite purple star.

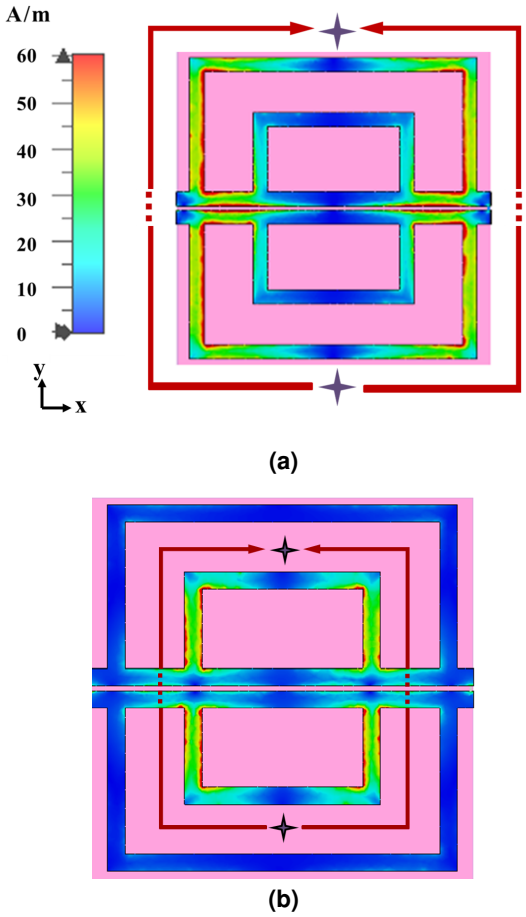


**Figure 13:** Surface current distribution at: (a) 2.45 GHz, (b) 5.2 GHz.

### 3.2. Super cell Design

Following the unit cell design, we study the supercell, the proposed dual-band supercell consists of 4 cells ($N = 4$) along the $x$-axis with a single resistive load. As in the case of the single-band design, first, the supercell is designed with an initial load value equal to that of the unit cell (300 Ω). In the next step, the load value needs to be reoptimized; contrary to the single-band design, where we only had to reoptimize it for a single frequency, here we need to find a single load value that is simultaneously good—but not necessarily optimal—for both targeted frequencies. The load value is found to be 140 Ω, which leads to a capturing efficiency of 85% at 2.46 GHz and 66% at 5.18 GHz. This corresponds to an increase in the capturing efficiency compared to its initial value of 66% at 2.45 GHz and 44% at 5.17 GHz for a load of 300 Ω.

### 3.3. Finite Array Design

Following the proposed design strategy, a finite array of 5 × 4 cells was designed and simulated. Fig. 14 depicts five rows

consisting of 4 single cells each; every row is terminated by a 140 Ω resistive load.

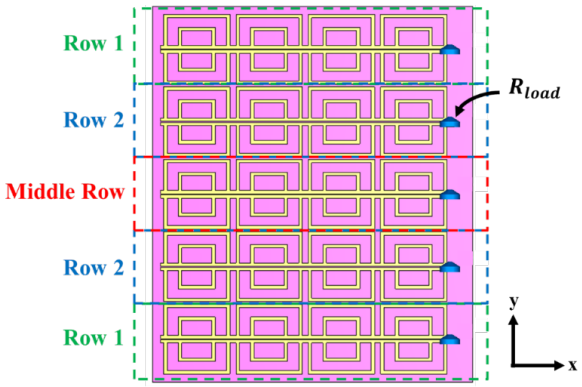


**Figure 14:** Finite array of 5×4 unit cells of the proposed dual-band metasurface harvester with row numbers.

As discussed for the single-band design regarding the finite array, the middle row and Row 2 exhibit a better performance at the targeted frequencies; as a result Fig. 15 presents only the capturing efficiency of these rows. Fig. 15 corresponds to the capturing efficiency with a resistive load of 140 Ω (reoptimized). The corresponding values are summarized in Table. 6.

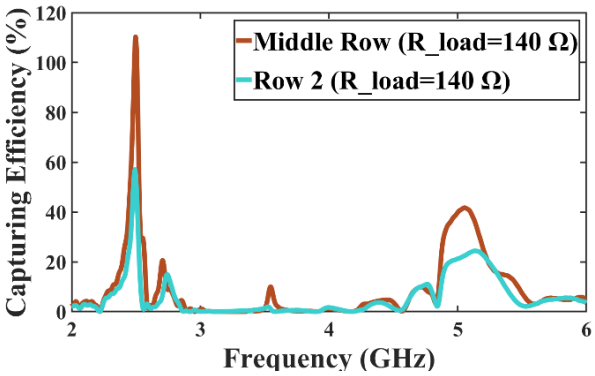


**Figure 15:** Simulated capturing efficiencies of the middle row and Row 2 of the proposed dual-band design corresponding to $R_{\text{load}} = 140\ \Omega$.

As in the single-band design, the capturing efficiency of the middle row of the dual-band design is higher than the one for Row 2. Comparing the performance of the middle row at 2.45 GHz and 5.2 GHz shows that the dual-band design is experiencing lower efficiency at the second frequency. Note that in comparison to the supercell, there is a more pronounced difference between the performance at 2.45 GHz and 5.2 GHz. This is because the array is of finite dimension, whereas the supercell is simulated in periodic ones.

Fig. 15 confirms that reoptimizing the resistive load leads to an enhancement in the capturing efficiency, as anticipated.

The middle row has the highest capturing efficiency at the two frequencies compared to the other rows. However, as discussed for the single-band harvester, the middle row is not a suitable representative for evaluating the performance of the design; rather, its adjacent rows (Row 2) should be considered as well. Indeed, central rows are more appropriate as they account for differences between the capturing efficiencies of its rows.

**Table 6:** Capturing efficiencies of different rows for the load of 140 Ω

| Row number | Frequency (GHz) | $\eta_{\text{MS}}$ (%) | Rload (Ω) |
|---|---|---|---|
| 2 | 2.5 | 57 | 140 |
| Middle | 2.5 | 110 | 140 |
| 2 | 5.12 | 25 | 140 |
| Middle | 5.04 | 42 | 140 |

Compared to the initial value of the load (300 Ω) of the unit cell, when the load is derived from the supercell optimization, the capturing efficiency of the average row of the proposed finite array increases from 53% at 2.5 GHz to 74% at 2.5 GHz, and from 24% at 5.13 GHz to 30% at 5.09 GHz, as shown in Fig. 16.

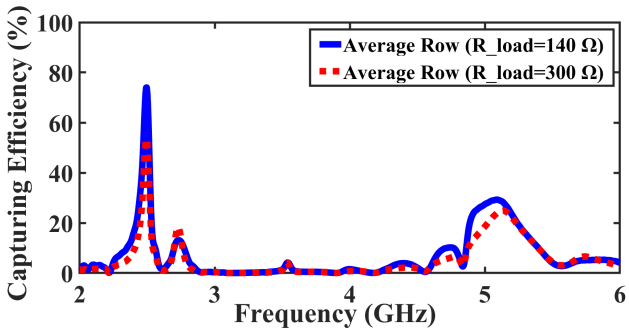


**Figure 16:** Simulated capturing efficiency of the average row for the initial $R_{\text{load}} = 300\,\Omega$ and the reoptimized $R_{\text{load}} = 140\,\Omega$.

In Fig. 16, the FWHM capturing bandwidth corresponding to the reoptimized load of 140 Ω is 0.064 GHz (2.456 to 2.52 GHz) for the low frequency and 0.518 GHz (4.872 to 5.39 GHz) for the high frequency. The corresponding Q-factors, calculated using Eq. 7, are 39 and 10. The higher Q-factor indicates a relatively narrower bandwidth at 2.5 GHz, whereas the lower Q-factor indicates a wider bandwidth at 5.2 GHz.

As the final step in analyzing the design performance, the discussion of fabrication and measurement of the proposed dual-band metasurface harvester is followed.

### 3.4. Realization and Measurement

Similar to the single-band design M1, the middle row of the metasurface finite array is chosen for measuring the capturing efficiency as its edge effects are minimal. A modification same as for the single-band metasurface design is made at the end of this row in order to measure the RF output power. However, except the middle row, the remaining rows are each terminated with a 150 Ω resistive load. The simulated capturing efficiency of the modified metasurface harvester is illustrated in Fig. 17. At 2.5 GHz, the capturing efficiency is 58%, with an FWHM of 0.058 GHz (2.472 GHz to 2.53 GHz) and a Q-factor of 43. At 5.1 GHz, the efficiency is 60%, with an FWHM of 0.248 GHz (4.98 GHz to 5.228 GHz), corresponding to a Q-factor of 20. The temporary modifications in the middle row

of the finite array led to an increase in efficiency at 5.1 GHz, while a decrease was observed at 2.5 GHz. This effect can be attributed to the fact that the unmodified dual-band design already showed a higher capturing efficiency at 2.5 GHz than at 5.1 GHz (Fig. 16), indicating better matching conditions with free space. Incorporating extension lines into the original design altered the matching condition at 2.5 GHz. Although this enhancement is beneficial at 5.1 GHz, it was unintended, as the extensions were introduced solely for preliminary metasurface measurements and are not a permanent part of the proposed design.

Nonetheless, we recognize that the performance at the second frequency requires further enhancement, which could be achieved by increasing the number of rows in the array, resulting in greater similarity between the array and the supercell in the sense that it is closer to the periodic boundary conditions implicit in the simulation of the supercell. Therefore it would be expected the larger array of the dual-band metasurface harvester to exhibit a higher capturing efficiency at the second frequency of 5.1 GHz (since the supercell showed a good performance at both frequencies.)

Fig. 17 further illustrates the sensitivity of the dual-band design's capturing efficiency to small variations in the lengths $b_1$ and $b_3$. At the low frequency of 2.5 GHz, the capturing efficiency changes by around 15% for each 0.1 mm increase in $b_1$, while the high frequency of 5.1 GHz remains unaffected by these changes, as shown in Fig. 17a. Conversely, the design shows less sensitivity to 0.1 mm variations in $b_3$ at 5.1 GHz, with the low frequency of 2.5 GHz remaining unchanged, as shown in Fig. 17b. While these length variations primarily affect the capturing efficiency, they cause only small shifts in the resonant frequencies — changes in $b_1$ result in small frequency shifts around 2.5 GHz, and changes in $b_3$ produce minimal shifts around 5.1 GHz. It is important to note that $b_1$ and $b_3$ are presented as representative parameters to highlight the design's sensitivity to these length changes. Other geometric factors, such as the line width and additional lengths like $b_2$ and $b_4$, may also influence the design's overall performance.

Fig. 18 depicts the simulated capturing efficiency of the average row (A.R.). Table. 8 provides the corresponding performance values. Additionally, Fig. 18 illustrates the simulated capturing efficiency of the average row under the oblique incidence angle of 20 degrees; this comparison plot shows that the proposed dual-band design has a good performance under an oblique incidence of 20 degrees (41% at 2.51 GHz and 33% at 5.11 GHz).

A dual-band metasurface harvester finite array consisting of 5 rows was fabricated on a 2.36 mm thick Arlon DiClad 880 dielectric substrate, as shown in Fig. 19a. As done for the single-band, to measure the collected RF power ($P_{dl}$) from the middle row of the dual-band design, a power sensor is used. The full measurement is performed similar to the single-band design. The gain of the horn and the emitted power by the generator for both frequencies are presented in Table. 7. Fig. 19b illustrates the comparison between the simulated average row and measured capturing efficiency under normal incidence; the corresponding values are summarized in Table. 8.

For the single-band design, the simulation, and measurement of the capturing efficiency reveal a good agreement at the low frequency. However, in the case of the dual-band design, the measured capturing efficiency at the low frequency is less than the simulated one. This difference can be attributed to that the dual-band design exhibits a narrower bandwidth at the low frequency, corresponding to a higher Q-factor for the average row of 46. However, the Q-factor for the average row in the single-band design is 27. As a result, the capturing efficiency of the dual-band design at the low frequency can be more sensitive with respect to dimensional variations (similar to the discussion in Fig. 17) and fabrication tolerances.

At the high frequency, however, the agreement between simulation and measurement is significantly better. This can be attributed to the wider bandwidth (lower Q-factor) of the dual-band design at said frequency, which reduces the sensitivity to dimensional variations and fabrication tolerance, thereby enhancing consistency between simulated and measured results.

Fabrication tolerances, such as variations in substrate thickness or permittivity, can contribute to frequency shifts. According to specifications provided on the substrate packaging (by the manufacturer), the substrate thickness has an error margin of $\pm 0.076mm$, while the permittivity varies by $\pm 0.02$. However,

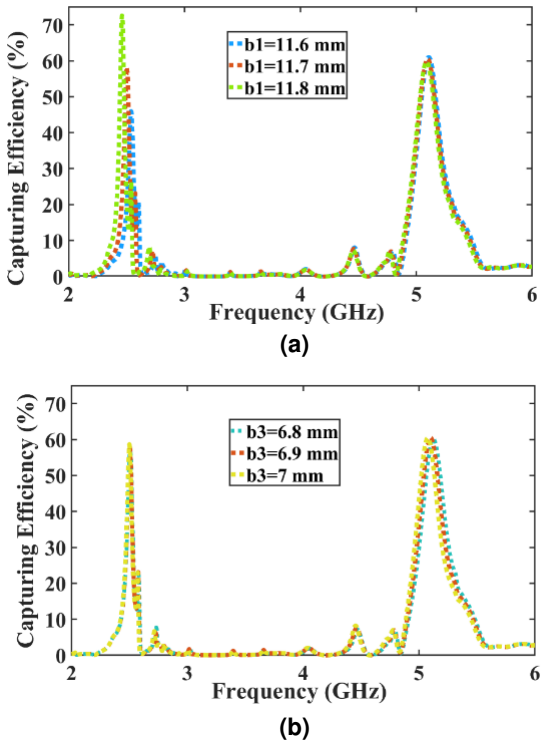


**Figure 17:** Simulated capturing efficiencies of the middle row of the modified finite array for (a) different lengths of $b_1$ and (b) different lengths of $b_3$.

**Table 7:** Transmitter and propagation parameters

| Frequency (GHz) | Gain of the horn (dBi) | Emitted power measured at the horn input (dBm) |
|---|---|---|
| 2.5 | 6.4 | 24.4 |
| 5.1 | 9.7 | 23.1 |

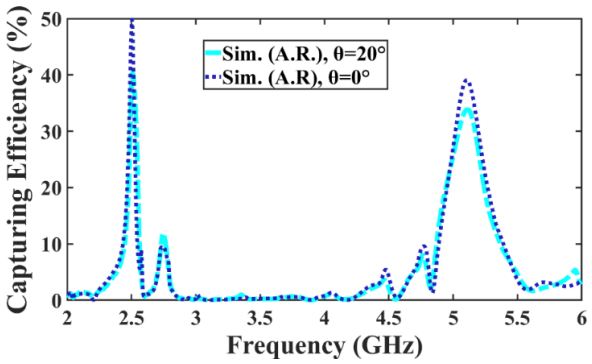


**Figure 18:** Comparison between simulated average row (A.R.) at different incidence angles.

**Table 8:** Performance values for simulated average row (A.R.) and measurement

| Sim/Meas. | $\eta_{MS}$ (%) | Freq (GHz) | FWHM ($\Delta f$) (GHz) | Q-factor | Step freq size (MHz) |
|---|---|---|---|---|---|
| Sim. (A.R.) | 49.8 | 2.5 | 2.474–2.528 (0.054) | 46 | 1 |
| Meas. | 25 | 2.47 | 2.4–2.51 (0.11) | 22 | 10 |
| Sim. (A.R.) | 40 | 5.1 | 4.95–5.268 (0.318) | 16 | 1 |
| Meas. | 38.5 | 5.05 | 4.92–5.31 (0.39) | 13 | 10 |

generally the measurement is in agreement with the proposal dual-band metasurface harvester design performance.

Table 10 summarizes some existing RF metasurface harvesters proposed in the state of art. The abbreviations used in Table 10 are defined in Table 9.

Our proposed design is not only compact, as is evident by comparison with [9], [10], [22], [23], [28], but it also uses the fewest lumped elements/rectifiers possible compared to [11], [22], [24]–[26], [28]–[30], [31]. In this paper compact single-layer single-band and dual-band metasurface harvesters whose capturing efficiency was improved by the proposed intermediate design step were analyzed in detail. We could show by our designs, that is more informative to consider central rows and not just evaluate the middle row.

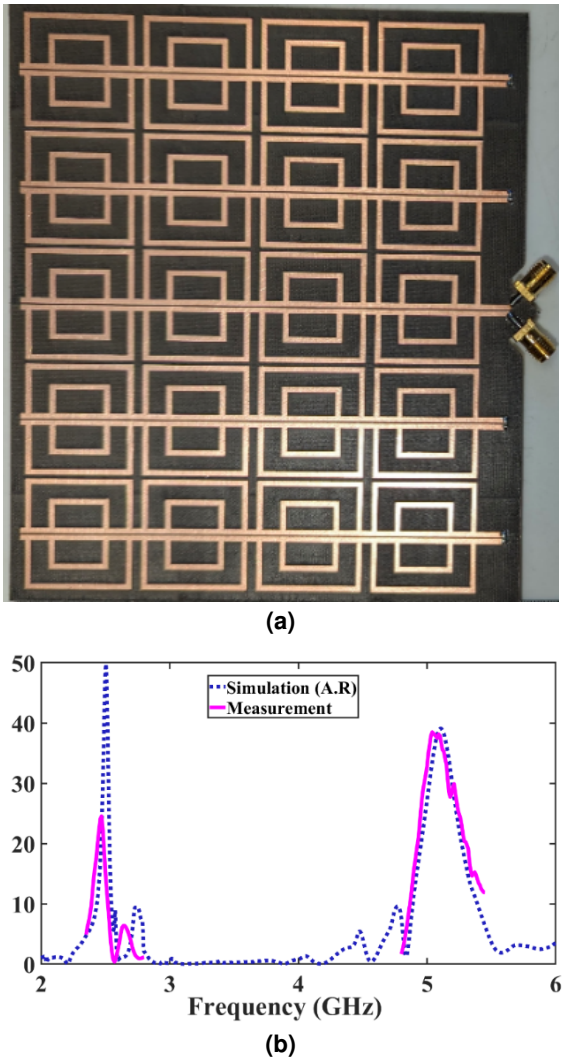


**Figure 19:** (a) Fabricated dual-band metasurface array, (b) Comparison between the simulated capturing efficiency of the average row (A.R.) and measured middle row at normal incidence.

## 4. Conclusion

In this work, compact efficient metasurface harvesters are proposed, analyzed, simulated, and measured individually without any implemented rectifier. Firstly, the single-band design operating at 2.45 GHz and then the dual-band design operating at 2.45 GHz, and 5.2 GHz. The additional step is suggested and applied for both proposed single and dual-band designs to improve the performance. A finite array of 5 × 4 cells is presented for both designs. The goal was to evaluate the performance of the metasurface design and to optimize its capturing efficiency. In contrast with typical ways of how works based on the interconnected cells method are presented - without discussing the measured capturing efficiency of their metasurface harvesters independently from the rectifier [9], [10], [22], [28] - we analyzed and measured the proposed metasurface harvesters alone. The proposed finite array was fabricated with the necessary modification to carry out the measurements. Taking into account the average row, an acceptable agreement was observed between the measured and the simulated capturing efficiencies under normal incidence. For the single-band design the latter peaks at 2.54 GHz with 73%, whereas the former is 61% at 2.49 GHz. For the dual-band design the simulated capturing efficiency peaks at 2.5 GHz with 49.8% and at 5.1 GHz with 40%, while the measured capturing efficiency at 2.47 GHz with 25% and at 5.05 GHz with 38.5%.

Deep evaluation of each proposed RF metasurface harvesters were provided and the advantages and disadvantages of them were discussed in detail. Additionally, we have proved that it is conceptually and practically simple to extend our single-band to a dual-band design. Based on this work, we conjecture that the design has the potential to be similarly extended to a triple-band design, namely by adding another resonator ring whose dimensions can be found following the design analysis.

**Table 9:** Abbreviations and Descriptions

| Abbreviation | Description |
|---|---|
| Ref | References |
| Freq | Frequency |
| R/C/Rect | Resistor / capacitor present / rectifier present |
| $\eta_{MS-c}$ | Unit cell capturing efficiency |
| Sim $\eta_{MS-s}$ / $\eta_{MS-AV}$ / $\eta_{MS-w}$ | Simulated capturing efficiency of the supercell / average row / whole finite array |
| Meas $\eta_{MS-MR}$ / $\eta_{MS-MC}$ / $\eta_{MS-Mw}$ | Measured capturing efficiency of the middle row / middle cell / whole finite array |
| WoN/WN | Without / with feed network |

**Table 10:** Performance comparison of some reported RF metasurface harvesters.

| Ref | Freq (GHz) | R/C/Rect | $\eta_{MS-c}$ (%) | Cell size (array) | **Sim** $\eta_{MS-s}$ / $\eta_{MS-AV}$ / $\eta_{MS-w}$ | **Meas** $\eta_{MS-MR}$ / $\eta_{MS-MC}$ / $\eta_{MS-Mw}$ |
|---|---|---|---|---|---|---|
| [20] | 3 | 1 R per cell (RF WN-Via used) | - | $0.153\lambda_0 \times 0.153\lambda_0$ (8×8) | $\eta_{MS-w}$ WoN/WN more than 80% | $\eta_{MS-Mw}$ WN 78% at 2.9 GHz |
| [21] | 2.4 | 1 R per cell (via used) | 97 | $0.2\lambda_0 \times 0.2\lambda_0$ (5×5) | - | $\eta_{MS-MC}$ 85% at 2.8 GHz |
| | 5.4 | | 94 | $0.45\lambda_0 \times 0.45\lambda_0$ (5×5) | | $\eta_{MS-MC}$ 83% at 5.43 GHz |
| [22] | 5.2 | 4 C per cell, 12 Rect. (in array) | - | $0.59\lambda_0 \times 0.59\lambda_0$ (6×6) | - | - |
| [11] | 2.4 | 2 Rect. per supercell (N=4) | 96 | $0.168\lambda_0 \times 0.168\lambda_0$ (7×7) | - | - |
| | 12.6 | | 92.9 | $0.882\lambda_0 \times 0.882\lambda_0$ (7×7) | | |
| [12] | 1.85 | 1 Rect. per supercell (N=4) | 86 | $0.21\lambda_0 \times 0.271\lambda_0$ (2-connected 4×5) | $\eta_{MS-s}$ 80% at 1.8 GHz | - |
| | 2.5 | | 83 | $0.283\lambda_0 \times 0.367\lambda_0$ (2-connected 4×5) | $\eta_{MS-s}$ 37% at 2.3 GHz | |
| This work | 2.45 | 1 R per supercell (N=4) | 88 | $0.22\lambda_0 \times 0.22\lambda_0$ (5×4) | $\eta_{MS-AV}$ * 74% at 2.5 GHz | - |
| | | | | | $\eta_{MS-AV}$ ** 49.8% at 2.5 GHz | $\eta_{MS-MR}$ 25% at 2.47 GHz |
| | 5.2 | | 92 | $0.47\lambda_0 \times 0.47\lambda_0$ (5×4) | $\eta_{MS-AV}$ * 30% at 5.09 GHz | - |
| | | | | | $\eta_{MS-AV}$ ** 40% at 5.1 GHz | $\eta_{MS-MR}$ 38.5% at 5.05 GHz |

* Without modification ** With modification

## References


**[1]** D.-J. Deng et al., "On quality-of-service provisioning in IEEE 802.11 ax WLANs," *IEEE Access*, vol. 4, pp. 6086–6104, 2016.

**[2]** D. Lopez-Perez et al., "IEEE 802.11 be extremely high throughput: The next generation of Wi-Fi technology beyond 802.11 ax," *IEEE Commun. Mag.*, vol. 57, no. 9, pp. 113–119, Sep. 2019.

**[3]** L. Li, X. Zhang, C. Song, and Y. Huang, "Progress, challenges, and perspective on metasurfaces for ambient radio frequency energy harvesting," *Appl. Phys. Lett.*, vol. 116, no. 6, Feb. 2020.

**[4]** J. Zhou, P. Zhang, J. Han, L. Li, and Y. Huang, "Metamaterials and metasurfaces for wireless power transfer and energy harvesting," *Proc. IEEE Inst. Electr. Electron. Eng.*, vol. 110, no. 1, pp. 31–55, 2021.

**[5]** O. M. Ramahi, T. S. Almoneef, M. Alshareef, and M. S. Boybay, "Metamaterial particles for electromagnetic energy harvesting," *Appl. Phys. Lett.*, vol. 101, no. 17, Oct. 2012.

**[6]** X. Zhang, H. Liu, and L. Li, "Electromagnetic power harvester using wide-angle and polarization-insensitive metasurfaces," *Appl. Sci.*, vol. 8, no. 4, Mar. 2018.

**[7]** X. Duan, X. Chen, and L. Zhou, "A metamaterial electromagnetic energy rectifying surface with high harvesting efficiency," *AIP Adv.*, vol. 6, no. 12, Dec. 2016.

**[8]** M. El Badawe, T. S. Almoneef, and O. M. Ramahi, "A metasurface for conversion of electromagnetic radiation to DC," *AIP Adv.*, vol. 7, no. 3, Mar. 2017.

**[9]** F. Erkmen, T. S. Almoneef, and O. M. Ramahi, "Scalable electromagnetic energy harvesting using frequency-selective surfaces," *IEEE Trans. Microw. Theory Techn.*, vol. 66, no. 5, pp. 2433–2441, May 2018.

**[10]** W. Li, T. Shen, B. Zhang, and Y. Wei, "A scalable, wide-angle metasurface array for electromagnetic energy harvesting," *Micromachines*, vol. 15, no. 7, p. 904, 2024.

**[11]** Y. Wei, J. Duan, H. Jing, H. Yang, H. Deng, C. Song, J. Wang, Z. Qu, and B. Zhang, "Scalable, dual-band metasurface array for electromagnetic energy harvesting and wireless power transfer," *Micromachines*, vol. 13, no. 10, p. 1712, Oct. 2022.

**[12]** F. Erkmen and O. M. Ramahi, "A scalable, dual-band absorber surface for electromagnetic energy harvesting and wireless power transfer," *IEEE Trans. Antennas Propag.*, early access, May 27, 2021.

**[13]** Y. Wei et al., "A multiband, polarization-controlled metasurface absorber for electromagnetic energy harvesting and wireless power transfer," *IEEE Trans. Microw. Theory Techn.*, vol. 70, no. 5, pp. 2861–2871, May 2022.

**[14]** Rogers Corporation, 2023, "DiClad® Series Laminates," [Online]. Available: https://www.rogerscorp.com/advanced-electronics-solutions/diclad-series-laminates/diclad-870_880-laminates

**[15]** R. Sharifi, A. C. Lepage, K. Niotaki, and X. Begaud, "A single-layer efficient metasurface absorber for RF energy harvesting applications," in *2025 IEEE Int. Workshop Antenna Technol. (iWAT)*, pp. 1–4, 2025.

**[16]** R. Sharifi, A. C. Lepage, K. Niotaki, and X. Begaud, "An efficient compact dual-band metasurface RF energy harvester," in *2025 IEEE 19th Eur. Conf. Antennas Propag. (EuCAP)*, 2025.

**[17]** K. Chang and L.-H. Hsieh, *Microwave Ring Circuits and Related Structures*, 2nd ed. New York, NY, USA: Wiley, 2004.

**[18]** N. Fernez et al., "Radiative quality factor in thin resonant metamaterial absorbers," *IEEE Trans. Microw. Theory Techn.*, vol. 66, no. 4, pp. 1764–1772, Apr. 2018.

**[19]** D. B. Stojanović, G. Gligorić, P. P. Beličev, M. R. Belić, and L. Hadžievski, "Circular polarization selective metamaterial absorber in terahertz frequency range," *IEEE J. Sel. Topics Quantum Electron.*, vol. 27, no. 1, Jan./Feb. 2021.

**[20]** M. El Badawe, T. S. Almoneef, and O. M. Ramahi, "A metasurface for conversion of electromagnetic radiation to DC," *AIP Adv.*, vol. 7, no. 3, Mar. 2017.

**[21]** A. A. G. Amer, N. Othman, S. Z. Sapuan, A. Alphones, M. F. Hassan, A. J. A. Al-Gburi, and Z. Zakaria, "Dual-band, wide-angle, and high-capture efficiency metasurface for electromagnetic energy harvesting," *Nanomaterials*, vol. 13, no. 13, p. 2015, Jul. 2023.

**[22]** M. Amiri, M. Abolhasan, N. Shariati, and J. Lipman, "Highly efficient polarization-insensitive EM energy harvester," in *Proc. 18th Eur. Conf. Antennas Propag. (EuCAP)*, pp. 1–5, Mar. 2024.

**[23]** Y. Wei et al., "A dual-band, polarization-insensitive, wide-angle metasurface array for electromagnetic energy harvesting and wireless power transfer," *Results Phys.*, vol. 46, Mar. 2023.

**[24]** F. Yu, X. Yang, H. Zhong, C. Chu, and S. Gao, "Polarization-insensitive wide-angle-reception metasurface with simplified structure for harvesting electromagnetic energy," *Appl. Phys. Lett.*, vol. 113, no. 12, Sep. 2018.

**[25]** M. Dinh, N. Ha-Van, N. T. Tung, and M. Thuy Le, "Dual-polarized wideangle energy harvester for self-powered IoT devices," *IEEE Access*, vol. 9, pp. 103376–103384, 2021.

**[26]** B. Ghaderi, V. Nayyeri, M. Soleimani, and O. M. Ramahi, "Pixelated metasurface for dual-band and multi-polarization electromagnetic energy harvesting," *Sci. Rep.*, vol. 8, no. 1, 2018.

**[27]** C. Song, Y. Wei, J. Kang, H. Jing, J. Wang, Z. Qu, B. Zhang, and J. Duan, "A dual-band, wide-angle absorbing metasurface for EM energy harvesting and wireless power transfer," *Opt. Commun.*, vol. 549, p. 129799, Dec. 2023.

**[28]** Y. Wei, J. Duan, H. Jing, Z. Lyu, J. Hao, Z. Qu, J. Wang, and B. Zhang, "A multiband, polarization-controlled metasurface absorber for electromagnetic energy harvesting

and wireless power transfer," *IEEE Trans. Microw. Theory Techn.*, vol. 70, no. 5, pp. 2861–2871, May 2022.

**[29]** W. Hu, Z. Yang, F. Zhao, G. Wen, J. Li, Y. Huang, D. Inserra, and Z. Chen, "Low-cost air gap metasurface structure for high absorption efficiency energy harvesting," *Int. J. Antennas Propag.*, vol. 2019, pp. 1–8, Sep. 2019.

**[30]** M. El Badawe, A. Albishi, and O. M. Ramahi, "Polarization independent dual-band RF energy harvester," in *12th Eur. Conf. Antennas Propag. (EuCAP)*, pp. 7–9, 2018.

**[31]** P. Shah and G. Shrikanth Reddy, "A dual-band, wide-angle, polarization insensitive metasurface-based RF energy harvester," in *2024 IEEE Int. Symp. Antennas Propag. INC/USNC-URSI Radio Sci. Meeting (AP-S/INC-USNC-URSI)*, pp. 1791–1792, 2024.